CLOUD FORMATION

Stratospheric air intrusions promote global-scale new particle formation

Jiaoshi Zhang[1], Xianda Gong[1], Ewan Crosbie[2,3], Glenn Diskin[2], Karl Froyd[4,5], Samuel Hall[6], Agnieszka Kupc[4,5,7], Richard Moore[2], Jeff Peischl[4,5], Andrew Rollins[5], Joshua Schwarz[5], Michael Shook[2], Chelsea Thompson[4,5], Kirk Ullmann[6], Christina Williamson[4,5,8,9], Armin Wisthaler[10,11], Lu Xu[1], Luke Ziemba[2], Charles A. Brock[5], Jian Wang[1]*

New particle formation in the free troposphere is a major source of cloud condensation nuclei globally. The prevailing view is that in the free troposphere, new particles are formed predominantly in convective cloud outflows. We present another mechanism using global observations. We find that during stratospheric air intrusion events, the mixing of descending ozone-rich stratospheric air with more moist free tropospheric background results in elevated hydroxyl radical (OH) concentrations. Such mixing is most prevalent near the tropopause where the sulfur dioxide (SO_2) mixing ratios are high. The combination of elevated SO_2 and OH levels leads to enhanced sulfuric acid concentrations, promoting particle formation. Such new particle formation occurs frequently and over large geographic regions, representing an important particle source in the midlatitude free troposphere.

New particle formation (NPF), a process involving vapor nucleation and subsequent formation of new particles, is a global-scale phenomenon in the free troposphere (*1*, *2*). In remote regions, new particles formed in the free troposphere often represent the dominant source of cloud condensation nuclei (CCN) in the boundary layer (*2*–*4*), thereby having a major influence on the properties of clouds and the radiative balance of the climate system. NPF has been frequently observed in the vicinity of convective clouds (*5*–*9*). The prevailing view is that in the remote free troposphere, new particles are formed predominantly in cloud outflow regions because convective clouds loft precursors (e.g., dimethyl sulfide) from the boundary layer and remove most of the preexisting particles that would otherwise compete with NPF as sinks for condensable vapors (*2*, *7*–*11*). However, several studies suggest that the frequently observed nucleation mode particles in the upper troposphere (UT) are unlikely to be fully explained by NPF associated with convective clouds (*12*, *13*). Newly formed particles have also been observed near the tropopause (*14*–*18*), a notable fraction of which are in mixtures of tropospheric and stratospheric air (*14*, *15*). Theoretical studies and box model simulations suggest that the NPF near the tropopause is due to the strong supersaturation created following the mixing of air masses with different relative humidities and temperatures (i.e., stratospheric and tropospheric air) (*13*–*16*, *19*). This supersaturation results from the curvature of temperature-dependent saturation vapor pressures of sulfuric acid (H_2SO_4) and water (*15*).

We present observational evidence of another NPF mechanism in the UT, using global airborne measurements [supplementary materials (SM) section M1] during NASA's North Atlantic Aerosols and Marine Ecosystems Study (NAAMES) (*20*) and Atmospheric Tomography (ATom) missions (*21*). We find that during stratospheric air intrusion events (SAI) (i.e., dynamic descent of stratospheric air into the troposphere), the mixing of descending stratospheric air and background tropospheric air leads to enhanced H_2SO_4 concentration and subsequent NPF. Because of the prevalence of SAI events, such NPF occurs frequently and over large geographic regions and likely represents an important source of particles in the free troposphere and by extension CCN in the remote marine boundary layer.

Particle formation in SAI-impacted air masses in the UT

A representative example of NPF in air masses influenced by SAI is shown in Fig. 1. Newly formed particles were observed at an altitude of ~7 km over the midlatitude North Atlantic on 4 September 2017 during NAAMES-3 under the conditions of elevated ozone (O_3) mixing ratios [>90 parts per billion (ppb)] and low relative humidity [(RH) <5%] and carbon monoxide (CO) mixing ratios (~100 ppb). The presence of newly formed particles is evident from [illegible] elevated concentration ratio of particles [illegible] diameters larger than 3 nm to those larger than 10 nm ($N_{>3nm}/N_{>10nm}$, Fig. 1B). In addition, the number fraction of particles that are volatile at 350°C is close to 100%, consistent with the volatile nature of recently formed particles in the atmosphere (*22*).

Elevated O_3 mixing ratios, low CO mixing ratios, and low RH in the free troposphere indicate influences by SAI (*23*–*25*), which is driven by downwelling at the extratropical tropopause (*26*). The SAI event is evident from the tongues of air (i.e., tropopause folds) penetrating the tropopause down to altitudes of ~5 km and lower (*23*, *27*, *28*) (Fig. 1E), which lead to strong influxes of stratospheric air with high O_3 mixing ratio and low RH and CO mixing ratios (*29*) (Fig. 1C). The newly formed particles coincide with elevated hydroxyl radical (OH) concentrations (Fig. 1B), which likely results from the mixing of descending stratospheric O_3-rich air with more moist tropospheric air (*30*, *31*). In addition, the air masses with elevated $N_{>3nm}/N_{>10nm}$ had been travelling at altitudes of ~10 km before descending to ~7 km, indicating that they had not been in recent contact with air from the lower troposphere or associated with any recent convective activities (*32*, *33*) (Fig. 1D). This evidence indicates that the mechanism of the NPF observed in the SAI-impacted air masses is different from the conventional one associated with outflow of convective clouds (*2*, *7*–*11*).

To differentiate NPF types, we used O_3 and water vapor (H_2O) mixing ratios as air mass tracers (*34*, *35*). NPF events were identified based on the condition $N_{>3nm}/N_{>10nm} > 1.3$ (*36*) (SM section M2) observed in the Northern Hemisphere (NH) midlatitude UT [20 to 60°N, 200 to 500 hectopascal (hPa)] (Fig. 2A). There are two different types of NPF events in the UT during NAAMES-3: One type is associated with elevated H_2O mixing ratios [> ~10^3 parts per million (ppm); Fig. 2B] in the vicinity of convective clouds (confirmed by videos recorded onboard the aircraft), consistent with the conventional picture that new particles are preferentially formed in the outflow of convective clouds (*8*, *10*). The relatively low O_3 mixing ratio during these NPF events also confirms the influence of air masses convectively transported from the lower free troposphere or the remote marine boundary layer (fig. S1) (*37*, *38*). In the second type, a large fraction of NPF events were observed in air masses with elevated O_3 (> ~70 ppb) but relatively low H_2O and RH levels, as shown in the example above (Fig. 1). These two types of NPF were also observed during the ATom-1 deployment over large geographic regions, specifically in the UT over the Northern Pacific and Atlantic oceans (Fig. 2C). Among the 57 NPF events over the Northern Pacific and Atlantic oceans during

[1]Center for Aerosol Science and Engineering, Department of Energy, Environmental and Chemical Engineering, Washington University in St. Louis, St. Louis, MO, USA. [2]NASA Langley Research Center, Hampton, VA, USA. [3]Science Systems and Applications, Inc., Hampton, VA, USA. [4]Cooperative Institute for Research in Environmental Sciences, University of Colorado, Boulder, CO, USA. [5]Chemical Sciences Laboratory, National Oceanic and Atmospheric Administration, Boulder, CO, USA. [6]Atmospheric Chemistry Observations and Modeling Laboratory, National Center for Atmospheric Research, Boulder, CO, USA. [7]Faculty of Physics, Aerosol Physics and Environmental Physics, University of Vienna, Vienna, Austria. [8]Climate Research Programme, Finnish Meteorological Institute, Helsinki, Finland. [9]Institute for Atmospheric and Earth System Research/Physics, Faculty of Science, University of Helsinki, Helsinki, Finland. [10]Institute for Ion Physics and Applied Physics, University of Innsbruck, Innsbruck, Austria. [11]Department of Chemistry, University of Oslo, Oslo, Norway.
*Corresponding author. Email: jian@wustl.edu

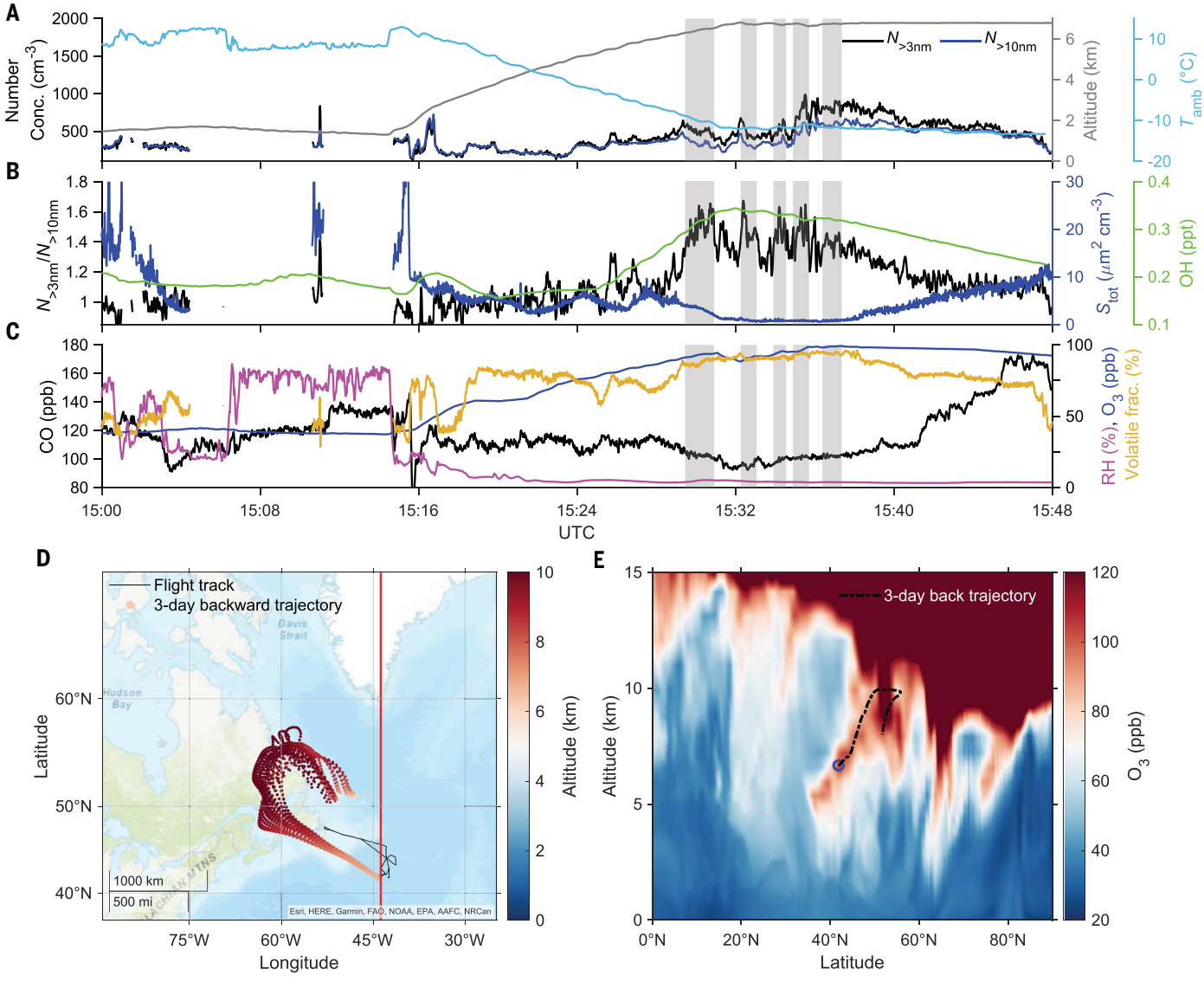

Fig. 1. Measurements onboard the C-130 aircraft in the upper troposphere (UT) impacted by stratospheric air intrusion on 4 September 2017. (**A**) Time series of number concentrations of particles larger than 3 nm ($N_{>3nm}$) and particles larger than 10 nm ($N_{>10nm}$), ambient temperature (T_{amb}), and flight altitude. (**B**) Time series of the concentration ratio of particles larger than 3 nm to particles larger than 10 nm ($N_{>3nm}/N_{>10nm}$), total particle surface area concentration (S_{tot}), and MERRA-2 GMI reanalysis hydroxyl radical (OH) mixing ratio. (**C**) Time series of measured carbon monoxide (CO) mixing ratio, relative humidity (RH), number fraction of particles volatile at 350°C, and MERRA-2 reanalysis ozone (O_3) mixing ratio. Periods of NPF events (i.e., $N_{>3nm}/N_{>10nm} > 1.3$) are highlighted using shading and in-cloud aerosol measurements are excluded (SM section M1). (**D**) Flight track of the C-130 aircraft (black line), longitudinal aircraft location during the period of NPF events (red line), and three-day backward air mass trajectories originating from the flight track during the NPF event period (UTC 15:29-15:38) colored by altitude. (**E**) Latitude–altitude cross section of O_3 mixing ratios from MERRA-2 reanalysis data during the NPF event period. The dashed line shows the mean air mass trajectory three days prior to arrival at the aircraft location (blue circle) during the period of NPF events.

ATom-1, 20 events were observed under increased O_3 (70 to 100 ppb) with enhanced OH mixing ratios [~0.77 part per trillion (ppt) on average]. Because air masses influenced by continental or biomass burning emissions are excluded from this analysis (SM section M1), the elevated O_3 is attributed to injection of stratosphere air (*39*) instead of photochemical production or lightning in the UT (*34*) (SM section S1 and fig. S2). The enhanced OH mixing ratio was observed preferentially in the air mass with moderately elevated O_3 instead of less-diluted stratospheric air with a much higher O_3 mixing ratio (Fig. 2D). This is consistent with previous model studies showing that the mixing of O_3-rich stratospheric air and more moist tropospheric air leads to enhanced OH abundance and thus higher oxidation capacity in the UT (*30*, *31*). We note that some of the air masses with elevated O_3 also exhibit high H_2O mixing ratios. This is because tropopause folds with deep vertical extent may occur in the vicinity of convective systems (*40*, *41*). Although stratospheric air is dry, the descending stratospheric air can mix with moist air convectively lofted from the lower troposphere, leading to relatively high H_2O mixing ratios in some cases (*42*, *43*).

Mechanism of NPF in SAI-impacted air masses

The vast majority of NPF with elevated O_3 levels was observed in the midlatitude UT. To further investigate potential mechanisms of the NPF in SAI-impacted air masses (hereafter SAI-NPF) and to statistically compare the characteristics of different NPF types, we identified

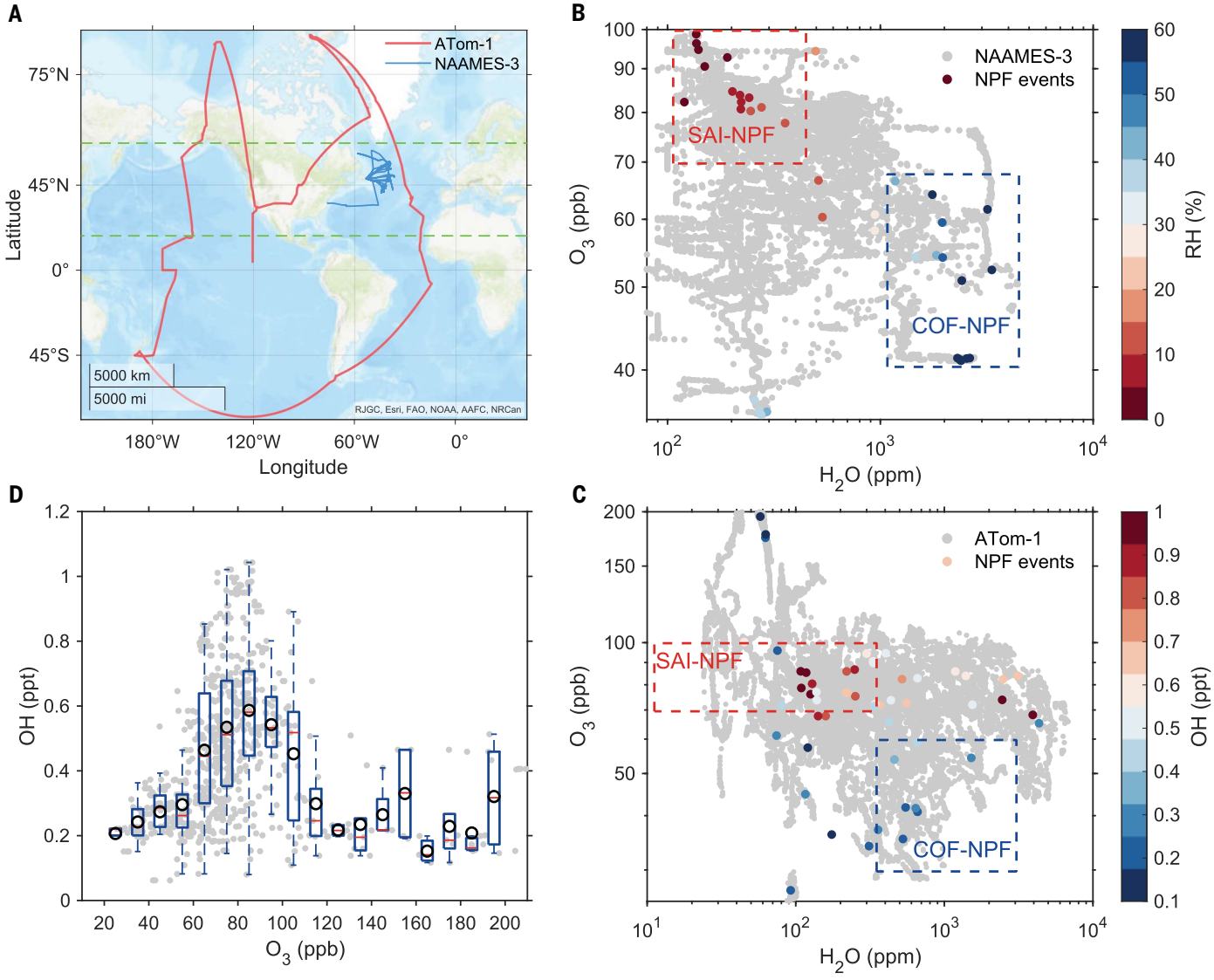

Fig. 2. Aircraft measurements of different new particle formation types in the UT over northern midlatitude oceans. (**A**) Flight tracks during the ATom-1 (July to August 2016) and NAAMES-3 (August to September 2017) deployments covering the midlatitude (i.e., 20 to 60° N, between the two green dashed lines) remote marine atmosphere over the northern Pacific and Atlantic oceans. (**B** and **C**) Ozone (O_3) mixing ratio versus water vapor (H_2O) mixing ratio (gray points) for all measurements in the UT (200 to 500 hPa) during NAAMES-3 (B) and over the northern Pacific and Atlantic Oceans (20 to 60° N) during ATom-1 (C). Measurements during NPF events are shown by dots colored according to relative humidity (RH) for NAAMES-3 (B) and hydroxyl radical (OH) mixing ratio for ATom-1 (C). NPF events observed in the stratospheric air intrusion (SAI) and convective cloud outflow (COF) air masses are grouped as SAI-NPF and COF-NPF, respectively. (**D**) Variation in OH mixing ratios as a function of O_3 mixing ratios in the UT over northern Pacific and Atlantic oceans during the ATom-1 deployment. Black circles represent the mean values and box-whisker plots are drawn for 10-, 25-, 50-, 75-, and 90-percentiles.

air masses influenced by SAI or convective cloud outflow (COF) in midlatitude UT based on the combination of O_3 and H_2O mixing ratios (SM section M3). Air masses with minimum influences from SAI and COF were classified as background-free troposphere (bgFT). All air masses and related NPF events in this study refer to those in the UT (200 to 500 hPa) over midlatitude oceans (20 to 60° N or 20 to 60° S) unless stated otherwise.

One possibility is that new particles in SAI-impacted air masses had already been formed in the stratosphere (*44*) and subsequently descended into the UT where they were observed. Most SAI-impacted NPF events during NAAMES-3 were observed at local solar noon (Fig. 3A), when strong solar radiation promotes the photolysis of O_3 and the production of OH (*45*). The occurrence of NPF mostly around solar noon suggests that these new particles were produced locally. The lifetime of new particles is relatively short (e.g., ~7 hours for 3 nm with typical coagulation sink in the UT), whereas it took 40 to 60 hours for the air masses to descend from ~10 km to the sampling altitudes (i.e., ~7 km). Therefore, few new particles that form at altitudes of 10 km or above survive the downward transport. In addition, given the long transport time, if these particles had formed in the stratosphere before being transported to the sampling location then it is unlikely that they were mostly observed around solar noon. Furthermore, given the general decreasing CO mixing ratio with altitude above 6 km (fig. S3), if the new particles formed at higher altitudes before being mixed downwards then we would observe a negative correlation between $N_{3\text{-}10nm}$ and CO mixing ratio, which is absent from the

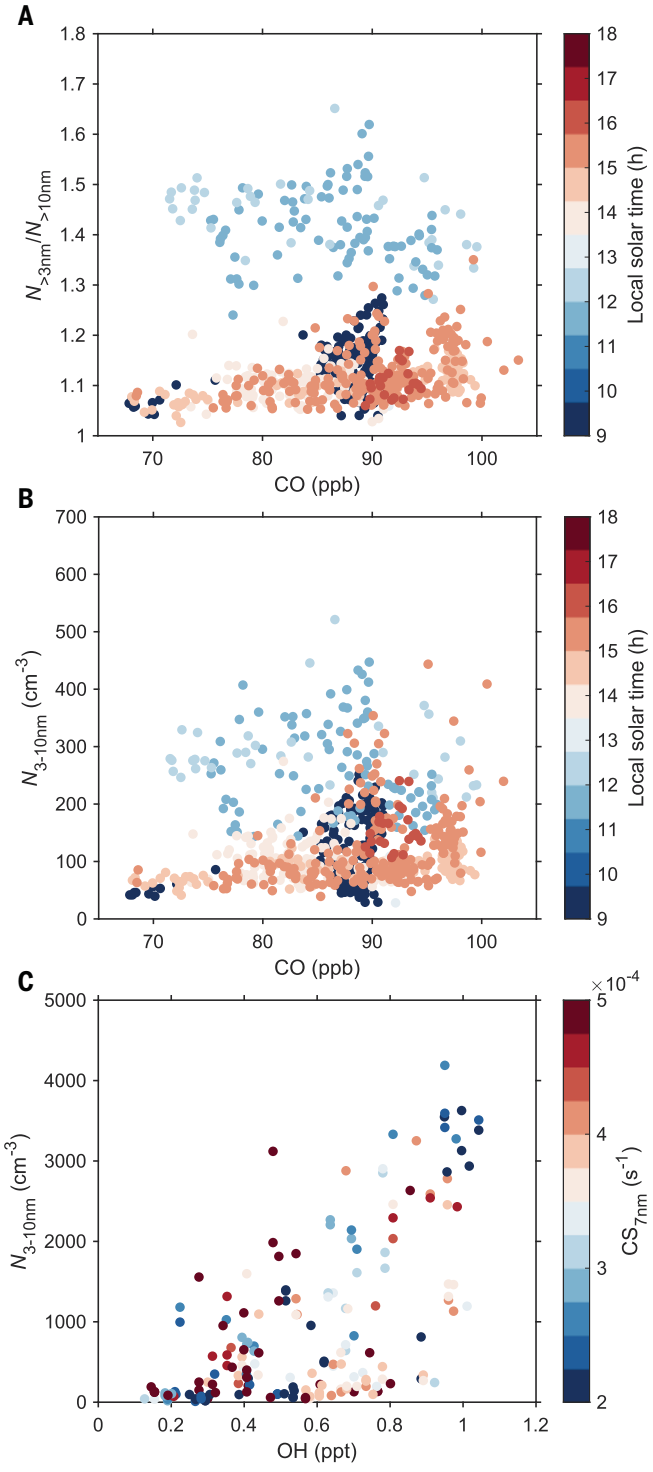

Fig. 3. New particles are formed in the mixture of stratospheric and tropospheric air locally instead of being transported from the stratosphere. (**A** and **B**) Scatter plots of $N_{>3nm}/N_{>10nm}$ (A) and $N_{3\text{-}10nm}$ (B) versus CO mixing ratio in air masses impacted by stratospheric air intrusion during NAAMES-3, with data points colored according to the local solar time (LSoT). LSoT is the time according to the position of the sun and the LSoT of 12 noon represents the time when the solar elevation angle reaches the maximum. CO denotes a tracer for anthropogenic emissions in the troposphere with a strong stratospheric sink. (**C**) Scatter plots of $N_{3\text{-}10nm}$ versus the OH mixing ratio in SAI-impacted air masses in the northern hemisphere during ATom-1, with data points colored according to the condensation sink for particles of diameters greater than 7 nm (CS_{7nm}). All data shown are from SAI-impacted air masses in the northern hemisphere UT over midlatitude oceans (20 to 60° N, 200 to 500 hPa).

measurements (Fig. 3B). Moreover, very few NPF events were observed in less diluted stratospheric air (SM section M3) with a much higher O_3 mixing ratio during ATom-1 (Fig. 2C). In SAI-impacted air masses, new particle concentration clearly correlates with OH mixing ratios (Fig. 3C).

Mixing of two air masses with different RH and temperatures could lead to strong supersaturation and enhanced nucleation rate (*19*) and it has been invoked to explain NPF observed near the tropopause (*15*, *16*). This mechanism could potentially contribute to the observed SAI-NPF. However, given that the mixing of the different air masses likely occurs throughout the day, the fact that newly formed particles were always observed around solar noon (Fig. 3, A and B) and with enhanced OH (Fig. 3C) suggests that photochemical reactions in the SAI-impacted air masses represent the key step leading to the NPF. The SAI-NPF is, to a large degree, due to enhanced OH and thus photochemistry, representing a different mechanism from the NPF in the outflow of convective clouds (*2*, *5*).

We estimated the impact of SAI on the nucleation rate in the UT using observations over northern midlatitude oceans during ATom-1. Earlier studies suggest that NPF in the UT is mostly through binary nucleation involving H_2SO_4 (*17*, *22*). The mean OH concentration during NPF events in the SAI-impacted air masses is ~6.60×10^6 cm^{-3}, roughly three times of that in the bgFT air masses (i.e., ~2.17×10^6 cm^{-3}). Over northern midlatitude oceans, the SO_2 mixing ratio during summer (e.g., ATom-1) is elevated at altitudes near the tropopause, peaking at ~11 km (fig. S4), possibly due to aircraft SO_2 emissions (*44*) and/or transport of tropospheric SO_2 through large-scale circulations including Asian summer monsoon (*46*) and flushing of the extratropical UT and lower stratosphere (*47*). As expected, SAI-impacted air masses are most prevalent near the tropopause (i.e., ~10 to 12 km over midlatitude oceans). As a result, SAI-impacted air masses tend to be at higher altitudes compared to the background tropospheric air masses. Because of the elevated SO_2 mixing ratios near the tropopause (SM section S2 and fig. S5), SAI-impacted air masses statistically have a higher SO_2 mixing ratio than the background tropospheric air (average 21.2 ppt versus 11.3 ppt, SM section M4 and fig. S6). Based on ATom-1 observations, the SAI-impacted air masses generally have a higher condensation sink for H_2SO_4 vapor from all particles with diameters greater than 7 nm (CS_{7nm}), compared to the free troposphere background (i.e., 3.27×10^{-4} s^{-1} versus 2.20×10^{-4} s^{-1}), likely due to higher aerosol mass loadings in the descending stratospheric air (*48*) (SM section S3 and fig. S7). Based on the above information, we estimated that on average, the

concentration of H_2SO_4 is enhanced by a factor of 3.5 in air masses influenced by SAI as a result of enhanced OH and SO_2 mixing ratios, despite an increase in CS_{7nm} (SM section M4). This results in a 110-fold increase in the estimated binary homogeneous nucleation rate in SAI-impacted air masses, reaching ~0.85 cm^{-3} s^{-1} under representative conditions (SM section M4 and table S1). The enhanced H_2SO_4 concentration and nucleation rate likely lead to the observed SAI-NPF. It has been suggested that oxidized organics may participate in NPF in the UT (*2*, *32*, *49*). The enhanced OH mixing ratio in SAI-impacted air masses is also expected to accelerate the formation of the oxidized organic species from their precursors, further increasing the nucleation rate. Based on simulations of GEOS-Chem-TOMAS (*50*), ammonia mixing ratio in the UT over global oceans is likely too low (i.e., 99th percentile of 6.2 ppt) for nitric acid to contribute substantially to the observed SAI-NPF (*51*).

The underlying mechanism of SAI-NPF, based on the results above, is illustrated in Fig. 4. The tropopause folds cause downward intrusion of stratospheric air with abundant O_3 into the troposphere. The mixing of intruding O_3-rich stratospheric air with more moist tropospheric air leads to enhanced OH mixing ratios. Such mixing is most prevalent near the tropopause, where the SO_2 mixing ratio is elevated during summer (figs. S4 and S5) (*52*). The elevated OH and SO_2 mixing ratios synergistically lead to an increase of H_2SO_4 concentration, promoting NPF (*22*). The stratospheric air intrusion can also bring the air with elevated SO_2 near the tropopause and the mixing of stratospheric and tropospheric air down to lower altitudes (e.g., ~7 km), leading to the NPF observed during NAAMES-3. This mechanism also helps explain previously reported NPF near the tropopause where the mixing of tropospheric and stratospheric air occurs (*14*–*16*).

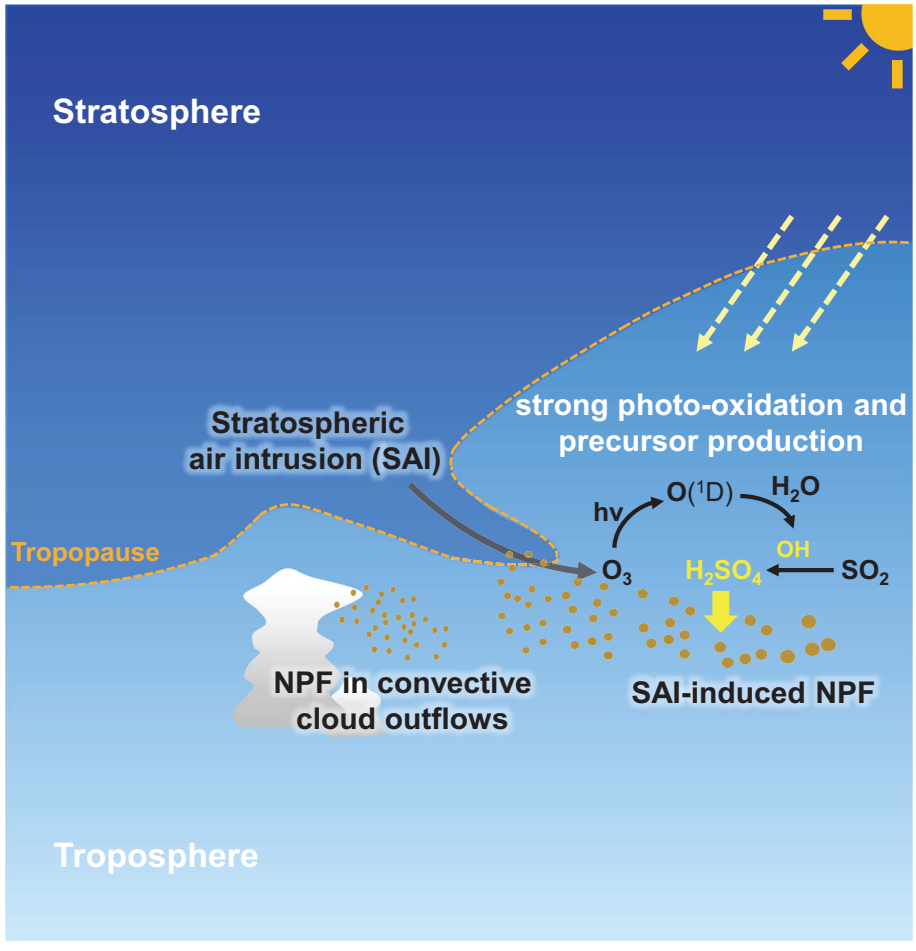

Fig. 4. Mechanism of new particle formation in the UT following the mixing of stratosphere and troposphere air. In the UT, intrusions of stratospheric air down into the troposphere occur as a result of tropopause folds. The mixing of O_3-rich stratospheric air with more moist tropospheric air enhances OH production in the presence of solar radiation, leading to elevated OH mixing ratio. Such mixing is most prevalent near the tropopause, where the SO_2 mixing ratio is elevated during summer. The elevated OH and SO_2 mixing ratios following the mixing synergistically lead to an increased H_2SO_4 concentration, promoting new particle formation. The stratospheric air intrusion can also bring air with elevated SO_2 near the tropopause and the mixing of stratospheric and tropospheric air down to lower altitudes, leading to NPF well below the tropopause. This mechanism likely represents an important source of particles in the midlatitude free troposphere.

Significance of SAI impacts on the UT NPF

We statistically compare the characteristics of aerosol populations during SAI-NPF events to those during NPF in COF air masses (hereafter COF-NPF). Figure 5, A and E shows the frequencies of SAI-NPF and COF-NPF as a function of altitude during the NAAMES-3 and ATom-1 deployments. SAI-NPF events were generally observed at higher altitudes than COF-NPF. During NAAMES-3, the frequency of SAI-NPF (SM section M2) increases with altitude, reaching ~6% at 7.5 km. During ATom-1, the research aircraft sampled at higher altitudes and these measurements show that the SAI-NPF frequency further increases to ~13% at above 10 km, likely due to more prevalent stratospheric influences at higher altitudes. The COF-NPF events were observed at altitudes ranging from 5 to 11 km during NAAMES-3 and ATom-1, with an average frequency of ~3.3% between altitudes of 5.5 and 7 km during NAAMES-3 and ~3.7% between altitudes of 7 and 10 km during ATom-1.

The statistics of $N_{3\text{-}10nm}$, $N_{>3nm}/N_{>10nm}$, and CS_{7nm} for COF-NPF events observed during NAAMES-3 and ATom-1 are generally consistent (Fig. 5). During NAAMES-3, SAI-NPF was observed below 7.5 km as a result of the operational ceiling of the aircraft, and the SAI-NPF had lower $N_{>3nm}/N_{>10nm}$ and $N_{3\text{-}10nm}$ compared to those during COF-NPF (Fig. 5, F and G), suggesting weaker particle production. The weaker particle production can be attributed, at least partially, to the higher CS_{7nm} in SAI-impacted air masses (Fig. 5H and fig. S7). The relatively lower CS_{7nm} value in COF air masses is due to the following two reasons: first, the convective clouds efficiently remove preexisting particles, leading to low CS_{7nm} in the outflow region (*2*); second, the SAI-impacted airmass has higher CS_{7nm} as a result of the influence of stratospheric air with high aerosol mass loadings (*48*) (SM section S3 and fig. S7). During ATom-1, SAI-NPF was observed at higher altitudes (i.e., >9 km). Despite generally lower $N_{>3nm}/N_{>10nm}$ ratios (Fig. 5B), $N_{3\text{-}10nm}$ of SAI-NPF is about 2 times higher than that of COF-NPF during ATom-1 (Fig. 5C), indicating stronger particle production. The stronger particle production during these SAI-NPF events, despite the larger CS_{7nm} than during COF-NPF events, is likely a result of a combination of colder temperatures at higher altitudes (Fig. 5A) and the enhanced OH and SO_2 leading to higher concentrations

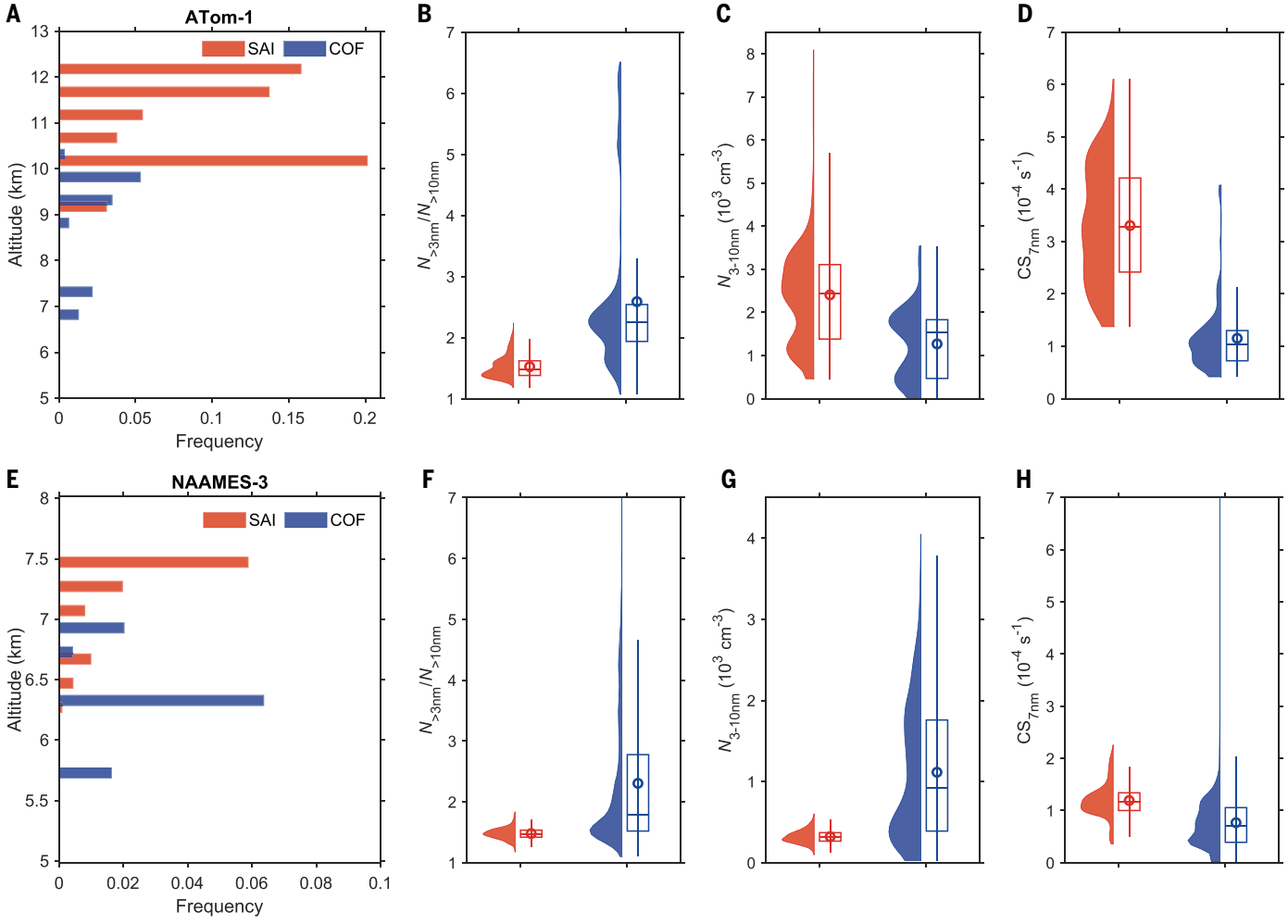

Fig. 5. Characteristics of SAI-NPF and COF-NPF events observed in the northern hemisphere UT over midlatitude oceans. (**A** to **D**) NPF frequency, defined as the ratio of the sampling time when new particles were observed to the total flight time for each 500-m altitude bin, as a function of altitude (A). Violin plots and boxplots showing $N_{>3nm}/N_{>10nm}$ (B), $N_{3\text{-}10nm}$ (C), and CS_{7nm} (D), of NPF events in SAI and convective cloud outflow (COF) air masses observed during the ATom-1 deployment. Circles represent the mean values and the box-whisker plots are drawn for 10-, 25-, 50-, 75-, and 90-percentiles. (**E** to **H**) are the same as (A to D) but for the NAAMES-3 deployment.

of nucleating species (e.g., H_2SO_4 and possibly oxidized organic species) in the SAI-impacted air masses. The high concentrations of H_2SO_4 and oxidized organics likely accelerate the growth of new particles and subsequent formation of CCN (*32*).

Based on the observations during all four ATom deployments, SAI-NPF occurs in the midlatitude UT over different seasons in both hemispheres (SM section S4 and fig. S8). The mixing ratio of OH shows strong seasonal variation, exhibiting the highest value during summer, mostly due to stronger solar radiation and a higher H_2O mixing ratio (fig. S9). The SAI-NPF frequencies in the NH during boreal fall and winter are lower than that during the boreal summer but are substantial, likely due to lower CS_{7nm} during the two seasons (fig. S10). In addition, the lower temperature during boreal winter also promotes NPF. Over the midlatitude oceans in the southern hemisphere (SH), the SAI-NPF frequencies in the UT are the highest during austral summer and fall (~6%). NPF events with elevated O_3 level were mostly observed over midlatitudes and this is attributed to the spatial distribution of SAI. Using the Modern-Era Retrospective Analysis for Research and Applications, Version 2 (MERRA-2) reanalysis dataset (SM section M5), we found that the SAI is most prevalent in the midlatitude regions, within the latitudinal band of 20° to 40°N and 20° to 40°S where the subtropical jet stream and synoptic-scale waves occur (*40*, *53*, *54*) (fig. S11). The zonally average mixing ratio of OH reaches the maximum in the midlatitudes (i.e., latitudinal bands of 20 to 40° N and 20 to 40° S) during summer for both NH and SH (fig. S12), consistent with the latitude range where both SAI frequency and solar radiation are high. Based on the ATom-1 and NAAMES-3 measurements, the fraction of data in SAI-impacted air masses (SM section M3) indicating recent NPF varies from ~5% at altitudes of 6.5 to 7.5 km to ~27% at altitudes of 10 to 12.5 km over northern midlatitude oceans during boreal summer. Measurements during ATom-2 show that the NPF frequency in SAI-impacted air masses is ~24% at altitudes of 10 to 11.5 km over southern midlatitude oceans during austral summer.

The results based on ATom observations show that the SAI-NPF likely occurs frequently over large geographic regions in the midlatitudes. Above 10 km, SAI-NPF is more frequent and leads to stronger production of new particles compared to the NPF associated with convective cloud outflow (Fig. 5). In addition, climate models predict a strengthening Brewer-Dobson circulation in future climate that would enhance stratosphere-to-troposphere transport, leading to more frequent SAI and increased magnitude of ozone flux (*55*, *56*). Therefore, NPF from SAI likely represents a key source of particles in the midlatitude free troposphere, both now and in the future. In the

tropics, deep convections can inject moist air from the troposphere into the lower stratosphere. We hypothesize the mixing of injected tropospheric air and lower stratospheric air may similarly result in enhanced OH, thereby enhancing NPF in the stratosphere over the tropics.

REFERENCES AND NOTES

1. H. Gordon *et al*., *J. Geophys. Res. Atmos.* **122**, 8739–8760 (2017).
2. C. J. Williamson *et al*., *Nature* **574**, 399–403 (2019).
3. A. D. Clarke *et al*., *Atmos. Chem. Phys.* **13**, 7511–7529 (2013).
4. F. Raes, *J. Geophys. Res.* **100**, 2893–2903 (1995).
5. A. D. Clarke *et al*., *J. Geophys. Res.* **103**, 16397–16409 (1998).
6. K. D. Perry, P. V. Hobbs, *J. Geophys. Res.* **99**, 22803–22818 (1994).
7. A. D. Clarke, V. N. Kapustin, F. L. Eisele, R. J. Weber, P. H. McMurry, *Geophys. Res. Lett.* **26**, 2425–2428 (1999).
8. D. C. Thornton, A. R. Bandy, B. W. Blomquist, J. D. Bradshaw, D. R. Blake, *J. Geophys. Res.* **102**, 28501–28509 (1997).
9. M. Kulmala *et al*., *J. Geophys. Res.* **111**, 2005JD006963 (2006).
10. C. H. Twohy *et al*., *Journal of Geophysical Research: Atmospheres* **107**, AAC 6-1–AAC 6-10 (2002).
11. A. Weigelt *et al*., *J. Geophys. Res.* **114**, 2008JD009805 (2009).
12. M. Hermann *et al*., *Tellus B Chem. Phys. Meterol.* **60**, 106–117 (2008).
13. A. Zahn *et al*., *J. Geophys. Res.* **105**, 1527–1535 (2000).
14. M. de Reus *et al*., *J. Geophys. Res.* **103**, 31255–31263 (1998).
15. F. Khosrawi, P. Konopka, *Atmos. Environ.* **37**, 903–910 (2003).
16. F. Schröder, J. Ström, *Atmos. Res.* **44**, 333–356 (1997).
17. C. A. Brock, P. Hamill, J. C. Wilson, H. H. Jonsson, K. R. Chan, *Science* **270**, 1650–1653 (1995).
18. R. Weigel *et al*., *Atmos. Chem. Phys.* **21**, 11689–11722 (2021).
19. E. D. Nilsson, M. Kulmala, *J. Geophys. Res.* **103**, 1381–1389 (1998).
20. NASA ASDC, NAAMES C-130 Aircraft Merge Data Files, EarthData ASDC (2022); https://doi.org/10.5067/ASDC/NAAMES_Merge_Data_1.
21. S. C. Wofsy *et al*., ATom: Merged Atmospheric Chemistry, Trace Gases, and Aerosols, Version 2, ORNL DAAC (2021); https://doi.org/10.3334/ORNLDAAC/1925.
22. E. M. Dunne *et al*., *Science* **354**, 1119–1124 (2016).
23. C. Appenzeller, H. C. Davies, *Nature* **358**, 570–572 (1992).
24. C. Appenzeller, H. C. Davies, W. A. Norton, *J. Geophys. Res.* **101**, 1435–1456 (1996).
25. K. E. Knowland, L. E. Ott, B. N. Duncan, K. Wargan, *Geophysical Research Letters* **44**, 10,691-10,701 (2017).
26. A. C. Boothe, C. R. Homeyer, *Atmos. Chem. Phys.* **17**, 5537–5559 (2017).
27. W. K. Hocking *et al*., *Nature* **450**, 281–284 (2007).
28. E. F. Danielsen, *J. Atmos. Sci.* **25**, 502–518 (1968).
29. Y. Gonzalez *et al*., *Atmos. Chem. Phys.* **21**, 11113–11132 (2021).
30. J. G. Esler *et al*., *J. Geophys. Res.* **106**, 4717–4731 (2001).
31. A. S. Kentarchos, G. J. Roelofs, *J. Geophys. Res.* **108**, 2002JD002598 (2003).
32. A. Kupc *et al*., *Atmos. Chem. Phys.* **20**, 15037–15060 (2020).
33. A. Stohl *et al*., *J. Geophys. Res.* **108**, 2002JD002490 (2003).
34. I. Bourgeois *et al*., *Proc. Natl. Acad. Sci. U.S.A.* **118**, e2109628118 (2021).
35. H. Flentje *et al*., *J. Geophys. Res.* **110**, 2004JD004957 (2005).
36. G. Zheng *et al*., *Nat. Commun.* **12**, 527 (2021).
37. S. J. Oltmans *et al*., *J. Geophys. Res.* **101**, 29,179–29,200 (1996).
38. E. N. Tinney, C. R. Homeyer, *J. Geophys. Res.* **126**, e2020JD033657 (2021).
39. J. L. Neu *et al*., *Nat. Geosci.* **7**, 340–344 (2014).
40. D. Akritidis, A. Pozzer, J. Flemming, A. Inness, P. Zanis, *J. Geophys. Res.* **126**, e2020JD034115 (2021).
41. Q. Tang, M. J. Prather, J. Hsu, *Geophys. Res. Lett.* **38**, L03806 (2011).
42. C. R. Homeyer, K. P. Bowman, L. L. Pan, M. A. Zondlo, J. F. Bresch, *J. Geophys. Res.* **116**, 2010GL046039 (2011).
43. J. R. Schroeder *et al*., *J. Geophys. Res.* **119**, 11,477–411,491 (2014).
44. C. J. Williamson *et al*., *Atmos. Chem. Phys.* **21**, 9065–9088 (2021).
45. R. S. Gao *et al*., *J. Atmos. Chem.* **71**, 55–64 (2014).
46. P. Yu *et al*., *Proc. Natl. Acad. Sci. U.S.A.* **114**, 6972–6977 (2017).
47. A. Gettelman *et al*., *Rev. Geophys.* **49**, 2011RG000355 (2011).
48. B. G. Martinsson *et al*., *J. Geophys. Res.* **110**, 2004JD005644 (2005).
49. J. Kirkby *et al*., *Nature* **533**, 521–526 (2016).
50. B. A. Nault *et al*., *Commun. Earth Environ.* **2**, 93 (2021).
51. M. Wang *et al*., *Nature* **605**, 483–489 (2022).
52. M. Höpfner *et al*., *Atmos. Chem. Phys.* **15**, 7017–7037 (2015).
53. J. Liu *et al*., *Atmos. Chem. Phys.* **20**, 6417–6433 (2020).
54. D. J. Ruiz, M. J. Prather, *Atmos. Chem. Phys.* **22**, 2079–2093 (2022).
55. M. Abalos *et al*., *Atmos. Chem. Phys.* **20**, 6883–6901 (2020).
56. W. J. Collins *et al*., *J. Geophys. Res.* **108**, 2002JD002617 (2003).
57. J. Zhang, Code: Binary nucleation rates in different air masses, Version v1, Zenodo (2024); https://doi.org/10.5281/zenodo.11113298.

ACKNOWLEDGMENTS

We thank NASA's NAAMES and ATom team, including the leadership team, science team, and pilots and crew for contributions to the airborne measurements. We are grateful to Paul O. Wennberg and Yuanlong Huang for discussion and suggestions. We acknowledge W. H. Brune, D. O. Miller, and A. B. Thames for the OH data and NOAA BC group for the BC measurements. **Funding:** J.W., J.Z., and X.G. were supported by the National Science Foundation (NSF) Division of Atmospheric and Geospace Sciences (grant no. AGS-2147747) and NASA Radiation Sciences Program (grant no. 80NSSC19K0618). K.F., A.K., J.P., A.R., J.S., C.T., C.W., and C.B. were supported by NASA's Earth System Science Pathfinder Program (grant no. NNH15AB12I) and by NOAA's Health of the Atmosphere and Atmospheric Chemistry, Carbon Cycle, and Climate (AC4) Programs. K.F., J.P., C.T., and C.W. were also supported in part by NOAA cooperative agreements (grant no. NA17OAR4320101 and NA22OAR4320151). A.K. was supported by the Austrian Science Fund FWF's Erwin Schrodinger Fellowship (grant no. J-3613). This work was also supported by NASA under awards NNX15AJ23G, NNX15AH33A, NNH13ZDA001N, NNX15AT90G, NNX15AG71A, 80NSSC19K0124, and 80NSSC18K0630. **Author contributions:** J.W. and J.Z. conceived and designed the study, with input from all other authors. E.C., G.D., K.F., S.H., A.K., R.M., J.P., A.R., J.S., M.S., C.T., K.U., C.W., A.W., and L.Z. carried out measurements, data reduction, and quality checks. J.Z. and J.W. led the data analysis and the writing, with major contributions from C.A.B., A.W., X.G., K.F., and further input from all other authors. **Competing interests:** The authors declare no competing interests. **Data and materials availability:** The airborne measurement dataset of NAAMES observations is publicly available in the NASA Atmospheric Science Data Center (*20*). The airborne measurement dataset of ATom observations is publicly available in the Oak Ridge National Laboratory Distributed Active Archive Center (*21*). MERRA-2 reanalysis datasets are available through https://disc.gsfc.nasa.gov, and MERRA2-GMI datasets are available through https://acd-ext.gsfc.nasa.gov/Projects/GEOSCCM/MERRA2GMI/. The code for calculating nucleation rates in different air masses is available in Zenodo (*57*).

SUPPLEMENTARY MATERIALS

science.org/doi/10.1126/science.adn2961
Materials and Methods
Supplementary Text
Figs. S1 to S13
Table S1
References (*58*–*89*)

Submitted 5 December 2023; accepted 13 May 2024
10.1126/science.adn2961